Simultaneous measurement of axial strain and temperature based on twisted fiber structure

Xinyue Jiang (姜昕越)[1], Ping Lu (鲁 平)[1,*], Yuan Sun (孙 远)[1], Hao Liao (廖 浩)[1], Deming Liu (刘德明)[1], Jiangshan Zhang (张江山)[2], and Hui Liao (廖 辉)[3]

[1]*School of Optical and Electronic Information, National Engineering Laboratory for Next Generation Internet Access System, Huazhong University of Science and Technology, Wuhan 430074, China*

[2]*Department of Electronics and Information Engineering, Huazhong University of Science and Technology, Wuhan 430074, China*

[3]*Enviromental Protection Science and Technology Co., Ltd., Wuhan 430070, China*

**Corresponding author: pluriver@mail.hust.edu.cn*

Received January 12, 2018; accepted February 1, 2018; posted online March 28, 2018

In this Letter, an alternative solution is proposed and demonstrated for simultaneous measurement of axial strain and temperature. This sensor consists of two twisted points on a commercial single mode fiber introduced by flame-heated and rotation treatment. The fabrication process modifies the geometrical configuration and refractive index of the fiber. Different cladding modes are excited at the first twisted point, and part of them are coupled back to the fiber core at the second twisted point. Experimental results show distinct sensitivities of 34.9 pm/με with 49.23 pm/°C and −36.19 pm/με with 62.99 pm/°C for the two selected destructive interference wavelengths.

OCIS codes: 060.2370, 060.2430, 120.3180.
doi: 10.3788/COL201816.040602.

Strain is an important criterion in the field of the safety assessment of engineering structures, which can be used for structural safety evaluation and damage location. Among numerous strain sensing methods, fiber optic sensing technology stands out due to their intrinsic merits, such as small size, immunity to electromagnetic interference, low cost, and high sensitivity, just to name a few. In the past few decades, different structures and devices based on fibers have been studied, such as fiber interferometer[1–3], fiber Bragg grating (FBG)[4], and long period fiber grating (LPFG)[5]. For fiber-grating-based sensors, strain changes the pitch and the photoelastic coefficient of the fiber grating, leading to the resonant wavelength shift. They have good repeatability, but show very low sensitivity, about 1.1 and 7.6 pm/με for FBG and LPFG, respectively. In-line fiber interferometers have relatively high sensitivity for single parameter sensing, but usually suffer severe cross-talk problems from temperature[6,7], which is a limiting factor for accurate measurement, especially when detecting a weak strain signal. Therefore, simultaneous measurement of strain and temperature is of vital importance in practical applications.

A variety of solutions have been put forward to achieve dual-parameter measurement of strain and temperature. Most common ways are to cascade two independent fiber devices, such as an FBG with a photonic crystal fiber (PCF) modal interferometer[8] and an LPFG with a high-birefringence fiber loop mirror[9]. These methods pose challenging problems of complex structure and high cost. An alternative way is to design special fiber structures, such as using an S-fiber taper in an FBG[10], where the peak of an FBG and the destructive interference wavelength of the S-taper show distinct sensitivities to strain and temperature. Although the fiber taper is sensitive to strain, the obstacle of this kind of sensors for application is that the tensile strength is low because its tiny taper waist restricts the strain measurement range.

In this Letter, we proposed and demonstrated an in-line Mach–Zehnder interferometer (MZI) based on the twisted fiber structure for simultaneous measurement of axial strain and temperature. Wavelengths of the two selected interference dips show strain sensitivities of 34.9 and 36.19 pm/με and temperature sensitivities of 49.23 and 62.99 pm/°C, respectively. Simultaneous measurement can be realized by using the coefficient matrix. The sensor is easy to fabricate, with a low cost and high sensitivity, so it has potential for applications in engineering.

Figure 1(a) illustrates the fabrication process of the proposed sensor head. First, 2 cm of the coating was stripped off from a standard single mode fiber (SMF, Corning SMF-28). Then, one end of the fiber was mounted on a fixed fiber holder, and the other end was mounted on a fiber rotator, whose revolving speed was controlled by an electro-motor. An oxy-hydrogen flame was utilized to heat the bare SMF, and the heating length is approximately 1 mm. The fiber was stretched with a slight longitudinal force in advance, which can keep the fiber straight while it is too small to produce substantial elongation of the fiber. After an 8–10 s warm-up, the fiber was softened and then was driven to rotate, thus creating a twisted point on the fiber. When the fiber was cooled down, the heater was moved to a new position by the translation stage. Repeating the steps as aforementioned, the second

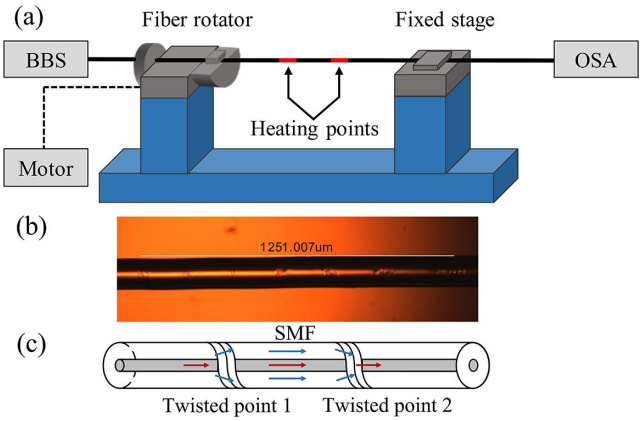

Fig. 1. (a) Fabrication process of the sensor head. (b) Microscopic image of the twisted area. (c) Basic structure of the sensor head.

twisted point can be obtained. Here, the twisted cycles and the distance between the two points are set to be 8 and 5 mm. Figure 1(b) is the microscopic image of the twisted sample. As can be seen, there is no obvious change in fiber diameter. The twist process brings about defects of the fiber and therefore modifies the geometrical configuration and refractive index (RI) of the fiber, effectively exciting some high-order cladding modes[11].

A schematic diagram is shown in Fig. 1(c) to explain the basic structure and working principle of the sensor head. Since the twist process modifies the RI distribution of the fiber, some cladding modes are excited at twisted point 1. Then, the remaining core mode and the cladding modes transmit along the fiber. When reaching twisted point 2, a fraction of the cladding modes are coupled back to the fiber core and interfere with the core mode, forming an in-line MZI.

For the circularly symmetric optical fiber, RI distribution along the fiber length is uniform, and modes inside the fiber are mutually orthogonal. So, the modes transmitting in a normal fiber cannot couple with each other. When the SMF is subjected to twist, the uniform RI distribution is broken, and mode coupling occurs. According to standard coupled mode theory[12], mode coupling derives from the special overlap integration of two modes. The coupling coefficient between two modes per unit length has the form

$$K_{p,q} = \frac{\omega}{4}\int_0^{\infty}\int_0^{2\pi} rE_p^*\tilde{\varepsilon}E_q \mathrm{d}\phi \mathrm{d}r = K_{q,p}^*, \tag{1}$$

where r and ϕ are the coordinates of a cylindrical reference frame, p and q are the different mode orders, E_p and E_q are their complete transverse electric fields, correspondingly. $\tilde{\varepsilon}$ is a 3×3 matrix representing the dielectric tensor of the fiber with a perturbation. Considering the twist, $\tilde{\varepsilon}$ can be written as

$$\tilde{\varepsilon} = g\tau\varepsilon_0 n_{av} r\begin{pmatrix} 0 & 0 & -\sin\phi \\ 0 & 0 & \cos\phi \\ -\sin\phi & \cos\phi & 0 \end{pmatrix}. \tag{2}$$

In Eq. (2), g is the elasto-optic coefficient of the fiber, τ represents the applied twist per unit length (twist rate), n_{av} is the mean RI, and ε_0 is the original dielectric tensor of the fiber without twist. Also, geometric configuration modification by twist changes the coupling matrix. As the fiber is rotated by an angle θ, the coupling matrix is transformed from K to $K' = R(\theta)KR^{\mathrm{T}}(\theta)$. $R(\theta) = \mathrm{diag}(R_{\mathrm{i}1}(\theta), R_{\mathrm{i}2}(\theta), \ldots)$ is a block-diagonal matrix. In a word, the above content implies that the twist fabrication process alters the coupling coefficient between modes and possibly excites different cladding modes under different twist parameters.

Suppose that more than one cladding mode participate in the interference, the transmission light intensity can be expressed as $I(\lambda) = I_{\mathrm{co}} + \sum_j I_{\mathrm{clad}}^j + 2\sum_j \sqrt{I_{\mathrm{co}} I_{\mathrm{clad}}^i}\cos(\varphi_j)$. Here, I_{co} and I_{clad} are the light intensity of the core mode and jth cladding mode. The phase difference between the core mode and jth cladding mode can be expressed as

$$\varphi_j = \frac{2\pi(n_{\mathrm{eff}}^{\mathrm{co}} - n_{\mathrm{eff}}^{\mathrm{cl},j})L}{\lambda} = \frac{2\pi}{\lambda}\Delta n_{\mathrm{eff}}^j L, \tag{3}$$

where $n_{\mathrm{eff}}^{\mathrm{co}}$, $n_{\mathrm{eff}}^{\mathrm{cl},j}$, and $\Delta n_{\mathrm{eff}}^i$ represent the effective RI of the core mode, the jth cladding mode, and the RI difference between them, respectively. λ is the wavelength of the propagating light, and L is the interference length of the proposed MZI (the distance between two twisted points). When ϕ_j reaches $(2m+1)\pi$, destructive interference will be formed. m is a positive integer, and the wavelength of the mth-order interference valley is given by

$$\lambda_m = \frac{2(n_{\mathrm{eff}}^{\mathrm{co}} - n_{\mathrm{eff}}^{\mathrm{cl},j})L}{2m+1} = \frac{2\Delta n_{\mathrm{eff}}^j L}{2m+1}. \tag{4}$$

The free spectral range is $\mathrm{FSR} = \lambda^2/2\Delta n_{\mathrm{eff}}^j L$. To obtain an applicable spectrum for measurement, L and the twist cycles should be carefully chosen. L affects both the FSR and the coupling coefficient of the sensor. On the one hand, FSR is inversely proportional to L. If L is too small, the FSR will be too large, so only a few interference valleys can be observed due to the limited light source wavelength range. On the other hand, high-order cladding modes, which are more sensitive to the ambient environment, are needed. However, they may suffer total loss if L is long enough. As for twist cycles, the more the cycles are, the bigger the modification of RI distribution is, which can excite a higher order of cladding mode. If the number of the twist cycles is changed, the twist rate τ is also varied, resulting in the exciting of the different-order modes and the alternations in the coupling coefficient between the core mode and the cladding modes. Nevertheless, a larger number of twist cycles brings about larger insertion loss

and less robustness. After several tests, the optimal L and twist cycles are selected to be 5 mm and 8, respectively.

When the strain is applied to the sensor, due to the elasto-optical effect and the elongation of the interferometer, the wavelength of the interference valleys will shift. Similarly, when temperature changes because of thermo-optic effect and the thermal expansion effect of the fiber $\Delta n_{\text{eff}}^{j}$ and L change too. Since different cladding modes have different sensitivities towards strain and temperature[11,13,14], the variations of strain and temperature can be discriminated, and simultaneous measurement can be realized by using the coefficient matrix. The shifts of the dips are expressed as

$$\begin{bmatrix} \Delta\lambda_{\text{dip}\,a} \\ \Delta\lambda_{\text{dip}\,b} \end{bmatrix} = \begin{bmatrix} K_{\varepsilon,\text{dip}\,a} & K_{T,\text{dip}\,a} \\ K_{\varepsilon,\text{dip}\,b} & K_{T,\text{dip}\,b} \end{bmatrix} \begin{bmatrix} \Delta\varepsilon \\ \Delta T \end{bmatrix}, \tag{5}$$

where $K_{\varepsilon,\text{dip}\,a}$, $K_{\varepsilon,\text{dip}\,b}$, $K_{T,\text{dip}\,a}$, and $K_{T,\text{dip}\,b}$ are the strain and temperature sensitivities for the two selected dips.

The experimental setup for measuring axial strain is schematically shown in Fig. 2. A broad band light source (BBS, wavelength ranging from 1250 to 1650 nm) and an optical spectrum analyzer (OSA, Yokogawa AQ6370c) are employed to monitor the real-time transmission spectrum. Two ends of the fiber sensor are clamped in a straight state by fiber holders of the fixed stage and a translation stage before the test. The original interval of the two fiber holders is set to be 20 cm. Four dips can be observed in Fig. 3(a). By analyzing the spatial frequency, it is confirmed that different cladding modes are excited, as shown in Fig. 3(b). Here, dips 1 and 2 are chosen to sense the strain variation.

Then, the translation stage is moved by rotating the micro-positioner at a step of 10 μm, corresponding to inducing 50 με to the sensor at a time. Figure 4(a) reveals the transmission spectrum, where strain increases from 0 to 1000 με, while the temperature is kept constant at 23°C

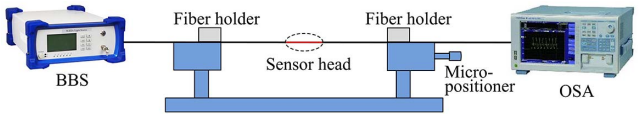

Fig. 2. Schematic of the experimental setup for strain measurement.

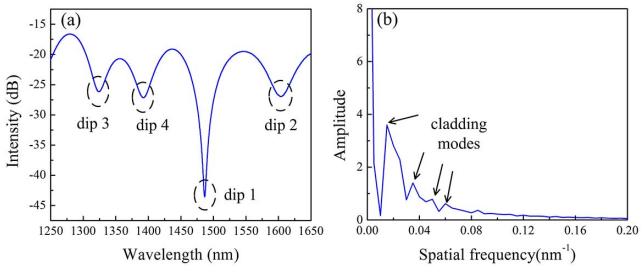

Fig. 3. (a) Initial transmission spectrum. (b) Spatial frequency after fast Fourier transform (FFT) transformation.

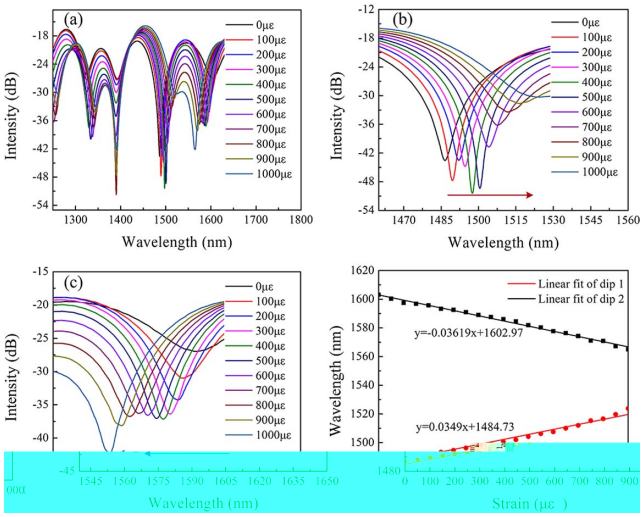

Fig. 4. (a) Transmission spectrum when strain increases from 0 to 1000 με. (b) Detailed information of dip 1. (c) Detailed information of dip 2. (d) Relationships between wavelength shifts and strain.

(room temperature). The detailed information for dips 1 and 2 are illustrated in Figs. 4(b) and 4(c). Dip 1 shifts to a longer wavelength, while dip 2 shifts to a shorter wavelength with the increment of the strain.

This phenomenon can be ascribed to the fact that for a twisted SMF, the shearing stress exists, and it induces the increment in the RI of the fiber, which can be written as $\Delta n = \frac{n_0^3 p_{44} \tau r}{2}$ [15]. At the twist points, the RI of the fiber core and the cladding will increase, and the variation of the effective RI of the cladding modes are more obvious than the core mode because of a larger radius. Because the heated point was twisted by eight cycles, each twisted point has periodic spiral structures with a very short length. When axial strain is applied, the twisted point is stretched, so the compressed material induced by twist will be elongated. This causes an obvious decrease for the RI of the cladding mode, while the RI of the core mode is considered to be unchanged due to the much smaller diameter. Moreover, the elasto-optical effect and the elongation of the interference length L are attributed to the experimental results as well. The elasto-optical coefficient of the germanium-doped fiber core is higher than that of the pure silica cladding; therefore, the decay of the RI of the core is more than that of the cladding modes as the strain is added. As a consequence, the wavelength shift is the result of the combination of the above principles. For dip 1, the effective RI difference $\Delta n_{\text{eff}}^{j}$ is positive because the $\Delta n_{\text{eff}}^{j}$ decrease induced by the elasto-optical effect is smaller than the $\Delta n_{\text{eff}}^{j}$ increment induced by twist. Along with the elongation of L, dip 1 shifts to a longer wavelength. For dip 2, $\Delta n_{\text{eff}}^{j}$ is negative because $\Delta n_{\text{eff}}^{j}$ decreasing by the elasto-optical effect is dominant; thus, the wavelength of dip 2 eventually blue shifts. The different wavelength shift directions of the two dips rely on the fact that

different-order cladding modes have distinct sensitivity characteristics, as mentioned in Ref. [13]. The wavelength variations as a function of axial strain are plotted in Fig. 4(d). Linear fit shows the strain sensitivities of 34.9 and −36.19 pm/με for dips 1 and 2, respectively, in the range of 0–1000 με, which are higher than many other fiber strain sensors reported in Refs. [2,5,16,17]. The intensity of the dips changes irregularly under different strain values, especially for dip 1. The primary reason is the nonuniform release of residual stress while heating. During the fabrication, the fiber is heated and twisted at the same time. Thus, the residual stress release along the fiber length can be uneven. This brings about the alternation of the coupling coefficient between modes. Finally, the energy of the dips will undergo obvious variation when the applied strain is changed. The temperature performance of the proposed sensor is also investigated. The fiber sensor head is put in the groove of the thermoelectric cooler (TEC) module with the temperature resolution of 0.1°C. Then, the sensor is heated from 20°C to 80°C at a step of 5°C, while the fiber is under a slight pre-strain of about 50 με. Dips 1 and 2 both undergo red shift monotonically as the temperature increases, which is shown in Figs. 5(a) and 5(b). Since different-order cladding modes have different thermo-optic coefficients, the two dips present the temperature sensitivities of 49.23 and 62.99 pm/°C, as shown in Fig. 5(c), by linear fit.

Several measurements of strain and temperature have been done, and the acquired sensitivities are very close to each other, which indicates that the sensor has good repeatability and stability.

The responses to strain and temperature of the other two dips in Fig. 3(a) are also tested. The results are depicted in Fig. 6. Dip 3 has the strain sensitivity of 30.69 pm/με in the range of 150 to 850 με. However, the wavelength of dip 3 does not change obviously when strain is less than 150 με and more than 850 με. Dip 4 is

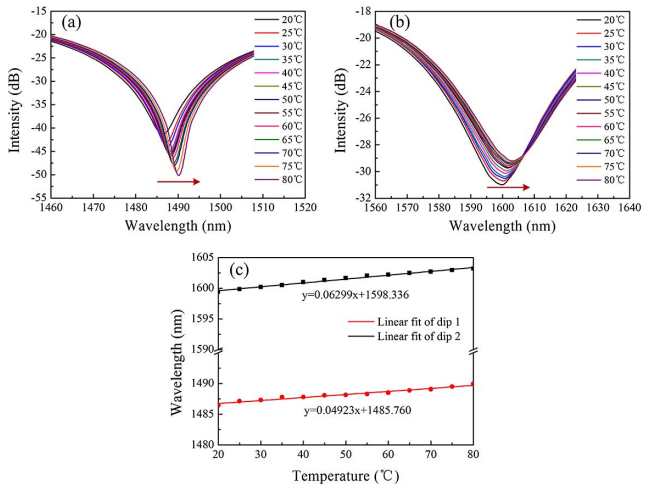

Fig. 5. (a) Wavelength shift of dip 1 as temperature increases. (b) Wavelength shift of dip 2 as temperature increases. (c) Relationships between wavelength shifts and temperature.

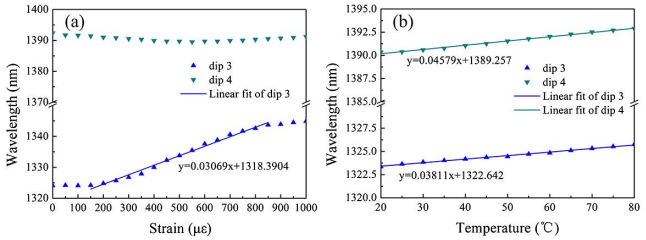

Fig. 6. Responses to the strain and temperature of dips 3 and 4.

not sensitive to the strain alternation. The temperature sensitivities of dips 3 and 4 are 38.11 and 45.79 pm/°C, respectively. To realize high-resolution dual-parameter measurement, the sensitivity difference between the two dips should be as large as possible. Dips 1 and 2 are selected for measurement because of the maximum sensitivity difference.

In this study, $K_{\varepsilon,\mathrm{dip1}}$, $K_{\varepsilon,\mathrm{dip2}}$, $K_{T,\mathrm{dip1}}$, and $K_{T,\mathrm{dip2}}$ are 34.9 pm/με, −36.19 pm/με, 49.23 pm/°C, and 62.99 pm/°C, respectively. As a consequence, the strain and temperature variations can be calculated as

$$\begin{bmatrix} \Delta\varepsilon \\ \Delta T \end{bmatrix} = \begin{bmatrix} 34.9 & 49.23 \\ -36.19 & 62.99 \end{bmatrix}^{-1} \begin{bmatrix} \Delta\lambda_{\mathrm{dip1}} \\ \Delta\lambda_{\mathrm{dip2}} \end{bmatrix}. \tag{6}$$

According to analysis in Ref. [18], the dual-parameter discrimination errors are determined by both the errors in the wavelength shift measurement and the errors in the transmission matrix elements. Considering the resolution of the OSA is 20 pm, the strain and temperature resolutions of ±0.564 με and ±0.357°C are obtained, which are higher than those in Refs. [4,8,9,17].

The capability of simultaneous measurement of strain and temperature is evaluated by applying strain variations at a fixed temperature (40°C) and temperature variations at a specific applied strain (500 με). The calculated and applied results are given in Fig. 7, which means the measured values calculated by the matrix show acceptable agreement with the applied values.

In summary, an approach to realize simultaneous measurement of strain and temperature based on a twisted

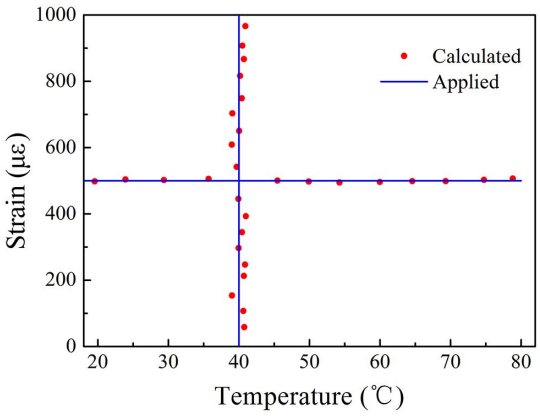

Fig. 7. Measured versus applied strain and temperature.

fiber structure is proposed and demonstrated. Experimental results show that the selected dips have sensitivities of 34.9 pm/με and −36.19 pm/με in the range of 0–1000 με for strain measurement and 49.23 pm/°C and 62.99 pm/°C in the range of 20°C–80°C for temperature measurement. Resolutions of dual-parameter sensing of strain and temperature are ±0.564 με and ±0.357°C by using the coefficient matrix. Therefore, the sensor proves relatively higher sensitivities and higher resolutions. In addition, such a sensor is easily fabricated, low-cost, and robust, providing the feasibility to be applied in the fields of safety assessment of engineering structures.

This work was supported by the National Natural Science Foundation of China (Nos. 61775070 and 61275083) and the Fundamental Research Funds for the Central Universities (No. 2017KFYXJJ032).

References

1. M. Hou, Y. Wang, S. Liu, Z. Li, and P. Lu, IEEE Sens. J. **16**, 6192 (2016).
2. R. M. André, C. R. Biazoli, S. O. Silva, M. B. Marques, C. M. B. Cordeiro, and O. Frazão, IEEE Photon. Technol. Lett. **25**, 155 (2013).
3. X. Zhang, H. Shao, H. Pan, Y. Yang, H. Bai, F. Pang, and T. Wang, Chin. Opt. Lett. **15**, 070601 (2017).
4. X. Shu, D. Zhao, L. Zhang, and I. Bennion, Appl. Opt. **43**, 2006 (2004).
5. Y. Ping, L. Xiao, D. N. Wang, and W. Jin, Opt. Lett. **31**, 3414 (2006).
6. X. Yan, H. Fu, H. Li, and X. Qiao, Chin. Opt. Lett. **14**, 030603 (2016).
7. C. Lin, Y. Wang, Y. Huang, C. Liao, Z. Bai, M. Hou, Z. Li, and Y. Wang, Photon. Res. **5**, 129 (2017).
8. B. Dong, J. Hao, C.-Y. Liaw, B. Lin, and S. C. Tjin, Appl. Opt., **49**, 6232 (2010).
9. O. Frazão, L. M. Marques, S. Santos, J. M. Baptista, and J. L. Santos, IEEE Photon. Technol. Lett. **18**, 2407 (2006).
10. J. Li, W. Zhang, S. Gao, Z. Bai, L. Wang, H. Liang, and T. Yan, IEEE Photon. Technol. **26**, 309 (2014).
11. Y. Sun, D. Liu, P. Lu, Q. Sun, W. Yang, S. Wang, L. Liu, and J. Zhang, IEEE Sens. J. **17**, 3045 (2017).
12. A. W. Snyder, J. Opt. Soc. Am. **62**, 1267 (1972).
13. X. Shu, L. Zhang, and I. Bennion, J. Lightwave Technol. **20**, 255 (2002).
14. L. V. Nguyen, D. Hwang, S. Moon, D. S. Moon, and Y. Chung, Opt. Express. **16**, 11369 (2008).
15. Z. Zhang, W. Shi, K. Gao, and Z. Fang, Chin. Opt. Lett. **2**, 565 (2004).
16. J. Zhou, Y. Wang, C. Liao, G. Yin, X. Xu, K. Yang, X. Zhong, Q. Wang, and Z. Li, IEEE Photon. Technol. Lett. **26**, 508 (2014).
17. P. Lu and Q. Chen, IEEE Photon. J. **2**, 942 (2010).
18. W. Jin, W. C. Michie, G. Thursby, M. Konstantaki, and B. Culshaw, Opt. Eng. **36**, 2272 (1997).